

# AEROTHERMODYNAMICS OF DESCENT SPACE VEHICLES AT STRONG COUPLED RADIATIVE-GASDYNAMIC INTERACTION

Surzhikov Sergey<sup>(1)</sup>, Andrienko Daniil<sup>(2)</sup>

<sup>(1)</sup> Institute for Problems in Mechanics RAS, 119526, Russia, Moscow, prosp. Vernadskogo 101 block1, surg@ipmnet.ru

<sup>(2)</sup> Moscow Institute of Physics and technology, 141700, Russia, Moscow region, Dolgoprudnii, Institutski per. 9, daniilandrienko@gmail.com

## ABSTRACT

Radiative-convective problem of heat transfer to spherical space vehicle (SV) resolves under assumption of viscous, heat-conductive, chemically disequilibrium gas with spectral absorption and emitting. The atmosphere composition is carbon dioxide and mixture CO<sub>2</sub>-N<sub>2</sub> (volume fractions is 97%-3%). Such atmospheric composition is corresponding to Martian atmosphere. The main goal of present work is comparison of convective and radiative heating of surface SV (from the front stagnation point up to back one) for typical entering for Martian atmosphere conditions, particularly for single points of Pathfinder trajectory [1]. The similar formulation of the problem was solved early (starting from 70<sup>th</sup> of previous century), but only for frontal area of SV [2-7], using simplified radiative heat transfer equations. The space agencies of different countries all over the world are imposing the new requirements to the aero thermodynamic construction of descending space vehicles for Solar System planet investigation. These requirements are dictated by exclusive standards for the necessity in new calculation data and its analysis. The examples of convective and radiative surface heating for SV of complex shape one can find in [8-11].

## 1. PROBLEM DESCRIPTION

Two dimension equation system for viscous, heat-conductive, chemically disequilibrium gas with spectral absorption and emitting is:

$$\frac{\partial \rho}{\partial t} + \text{div } \rho \mathbf{V} = 0 \quad (1)$$

$$\begin{aligned} \frac{\partial \rho u}{\partial t} + \text{div } \rho u \mathbf{V} = & -\frac{\partial p}{\partial x} - \frac{2}{3} \frac{\partial}{\partial x} \mu \text{div} \mathbf{V} + \\ & + \frac{1}{r} \frac{\partial}{\partial r} \left[ r \mu \left( \frac{\partial v}{\partial x} + \frac{\partial u}{\partial r} \right) \right] + 2 \frac{\partial}{\partial x} \left( \mu \frac{\partial u}{\partial x} \right) \end{aligned} \quad (2)$$

$$\begin{aligned} \frac{\partial \rho v}{\partial t} + \text{div } \rho v \mathbf{V} = & -\frac{\partial p}{\partial r} - \frac{2}{3} \frac{\partial}{\partial r} \mu \text{div} \mathbf{V} + \\ & + \frac{\partial}{\partial x} \left[ \mu \left( \frac{\partial v}{\partial x} + \frac{\partial u}{\partial r} \right) \right] + 2 \frac{\partial}{\partial r} \left( \mu \frac{\partial v}{\partial r} \right) + 2 \mu \frac{\partial}{\partial r} \left( \frac{v}{r} \right) \end{aligned} \quad (3)$$

$$\begin{aligned} \rho c_p \frac{\partial T}{\partial t} + \rho c_p \mathbf{V} \text{grad} T = & \text{div } \lambda \text{grad} T + \frac{\partial p}{\partial t} + \\ & + \mathbf{V} \text{grad} p + \mu \left[ 2 \left( \frac{v}{r} \right)^2 + 2 \left( \frac{\partial v}{\partial r} \right)^2 + 2 \left( \frac{\partial u}{\partial x} \right)^2 \right] + \\ & + \mu \left[ \left( \frac{\partial v}{\partial x} + \frac{\partial u}{\partial r} \right)^2 - \frac{2}{3} \left( \frac{\partial u}{\partial x} + \frac{\partial v}{\partial r} + \frac{v}{r} \right)^2 \right] - \end{aligned} \quad (4)$$

$$\begin{aligned} -\text{div} \mathbf{q}_R - \sum_{i=1}^{N_s} h_i \dot{w}_i + \sum_{i=1}^{N_s} \rho c_{p,i} D_i \text{grad} Y_i \cdot \text{grad} T \\ \frac{\partial \rho_i}{\partial t} + \text{div } \rho_i \mathbf{V} = -\text{div} \mathbf{J}_i + \dot{w}_i, \quad i = 1, 2, \dots, N_s \end{aligned} \quad (5)$$

$$\frac{\partial \rho_m e_{v,m}}{\partial t} + \text{div } \rho_m \mathbf{V} e_{v,m} = \dot{e}_{v,m}, \quad m = 1, 2, \dots, N_v \quad (6)$$

where  $t$  – time;  $u, v$  – velocity  $\mathbf{V}$   $x$ -projection and  $r$ -projection;  $p, \rho$  – pressure and density;  $\mu$  – viscosity dynamic coefficient,  $T$  – translational particle motion temperature;  $\lambda$  – heat conductive coefficient;

$c_p = \sum_i^{N_s} Y_i c_{p,i}$  – specific mixture heat capacity at constant pressure;  $Y_i = \rho_i / \rho$  – mass fraction of  $i$ -mixture component;  $c_{p,i}, h_i, \rho_i$  – specific heat capacity at constant pressure, enthalpy and density of  $i$  mixture component;  $\dot{w}_i$  – chemical transformation mass rate for  $i$ -mixture component;  $D_i$  – diffusion coefficient of  $i$ -mixture component;  $\mathbf{J}_i$  – diffusion flux density of  $i$ -mixture component;  $\mathbf{J}_i = -\rho D_i \text{grad} Y_i$ ;  $N_s$  – number of chemical gas mixture components;  $e_{v,m}$  – specific vibrational energy of  $m$ -vibrational mode (all vibrational modes are numerated in single table, see table 1:  $\rho_m$  – molecules density at  $m$ -vibrational mode);  $\dot{e}_{v,m}$  – the specific vibrational  $m$ -mode changing rate (due to vibrational-translational (VT) energy exchange

and dissociation and recombination process). Vibrational mode characteristics are presented in table 1. Mass rate of  $i$ -component formation is calculated according to:

$$\dot{W}_i = M_i W_i,$$

where  $M_i$  – molecular weight of  $i$ -component,

$$W_i = \sum_{n=1}^{N_r} \left( \frac{dX_i}{dt} \right)_n = \sum_{n=1}^{N_r} \left( k_{f,n} b_{i,n} - a_{i,n} \prod_j X_j^{a_{j,n}} \right) - \sum_{n=1}^{N_r} \left( k_{r,n} b_{i,n} - a_{i,n} \prod_j X_j^{b_{j,n}} \right) \quad (7)$$

$a_{i,n}, b_{i,n}$  – stoichiometric coefficients of  $n$ -chemical reaction at generalized formulation:

$$\sum_{j=1}^{N_s} a_{j,n} [X_j] = \sum_{j=1}^{N_s} b_{j,n} [X_j], \quad n = 1, 2, \dots, N_r,$$

$X_i$  – volume-molarity concentration of  $i$ -component;  $[X_j]$  – chemical symbol of chemical reaction reagents and products;  $N_r$  – number of chemical reactions;  $k_{f,n}, k_{r,n}$  – rate constant of forward and backward reactions

$$k_{f(r),n} = A_{f(r),n} T^{n_{f(r),n}} \exp \left( -\frac{E_{f(r),n}}{kT} \right), \quad (8)$$

where  $A_{f(r),n}, n_{f(r),n}, E_{f(r),n}$  – constant rate approximating coefficient for forward ( $f$ ) and backward ( $r$ ) chemical reactions.

The diffusion, viscosity, heat conductivity efficient coefficients are calculated through approximating relations [12–14]. The collision integrals are calculated through approximation relation [15], and thermodynamic properties according to [16].

The radiative heat transfer equation is formulated in generalized form

$$\Omega \frac{\partial J_{\omega}(\mathbf{r}, \Omega)}{\partial \mathbf{r}} + \kappa_{\omega}(\mathbf{r}) J_{\omega}(\mathbf{r}, \Omega) = j_{\omega}(\mathbf{r}) \quad (9)$$

Here  $J_{\omega}(\mathbf{r}, \Omega)$  – the spectral intensity of radiation;  $\kappa_{\omega}(\mathbf{r})$  – spectral absorption coefficient;  $j_{\omega}(\mathbf{r})$  – spectral emitting coefficient, calculated through Kirchhoff law (under local thermodynamic assumption):

$$j_{\omega}(\mathbf{r}) = \kappa_{\omega}(\mathbf{r}) J_{b,\omega}(\mathbf{r}), \quad (10)$$

where  $J_{b,\omega}(\mathbf{r})$  – black body intensity of radiation (the Plank function);  $\mathbf{r}$  – radius-vector of current spatial coordinate;  $\Omega$  – unit vector along direction of radiation propagation. The intensity integration through directions (with the weight  $\Omega$ ) and through wave number gives the radiation flux density vector

$$\mathbf{q}_R = \mathbf{q}_R(\mathbf{r}) = \int_{4\pi} d\Omega \int_{\Delta\omega_{tot}} \Omega J_{\omega}(\mathbf{r}, \Omega) d\omega.$$

The kinetic model of gases CO<sub>2</sub>-N<sub>2</sub> mixture is given and carefully analyzed in [17]. Calculations performed under Maxwell-Boltzmann model of chemical reactive gases mixture thermodynamic state.

The spectral and group properties of high temperature complicated mixture of gases were calculated with program code ASTEROID [18]. The spectral absorption coefficient is presented as 97-groups model in the spectral range of wave number  $\Delta\Omega = 1000$ –150000 cm<sup>-1</sup>. The spectral absorption coefficient was averaged over rotational structure in the range  $\Delta\omega = 20$  cm<sup>-1</sup> during spectral groups characteristics calculating. The electronic bands, listed in table 2 are taken into account.

The radiation processes with electrons have not been taken into account due to relative small ionization. For integral flux density calculation the Ray-tracing method was used. In every spectral group the integration of heat transfer equation over 160 rays for each surface point was performed. The finite-difference mesh along every ray was generated through regular sampling method [19].

The radiation efficiency for electronic-vibrational bands of diatomic molecules is calculated, taking into account the difference between translational and vibrational temperature.

The Navier-Stokes equation is integrated with AUSM finite-different scheme of 1<sup>st</sup> and 2<sup>nd</sup> order of accuracy for spatial coordinates [20]. The nonuniform structured O-type meshes are used.

## 2. RESULTS

The flow and radiative-convective heating of spherical body in Martian atmosphere are calculated for three points of Martian space vehicle Pathfinder, the parameter are given in [1] and in table 3.

The trajectory point  $t=52$  s takes the intermediate position about equilibrium. This point is chosen for future calculations also because it is close to heating maximum. The numerical grid and stream lines for the second trajectory point are shown on fig. 1a. The field of  $V_y$  velocity and translational temperature are shown

on fig.2a-2d. One can see the main structural features of the flow field: the head shock wave, back-vortex flow in the vicinity of the rear stagnation line current, near and far wake region.

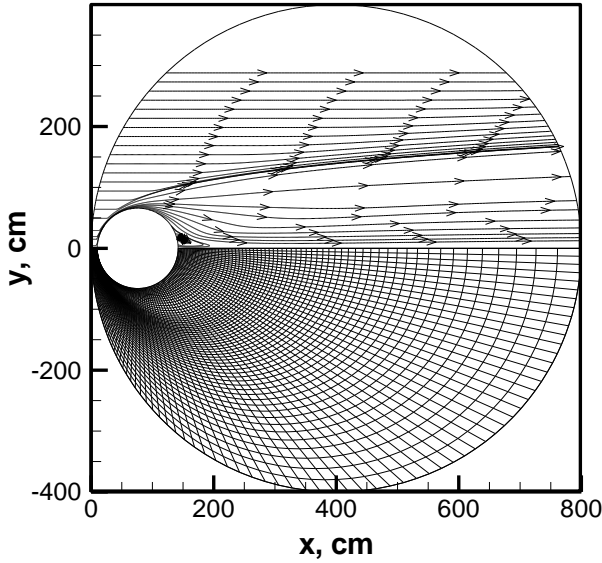


Fig. 1a. Stream lines of sphere flow with CO<sub>2</sub> and N<sub>2</sub> mixture at trajectory point  $t=52$  s. Mesh 141x61 nodes.

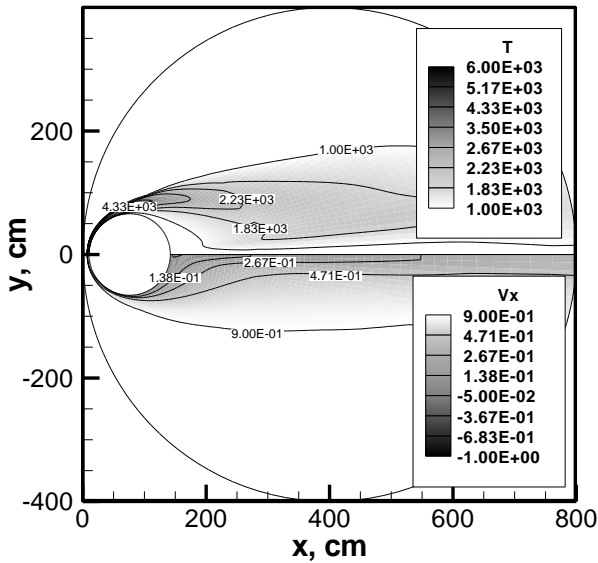


Fig. 1b. The longitudinal velocity  $V_x = u/V_\infty$  and temperature of sphere flow with CO<sub>2</sub> and N<sub>2</sub> mixture at trajectory point  $t=52$  s. Mesh 141x61 nodes.

The axial distribution of temperature along the front crucial line is shown on fig. 2a, 2b and 2c. The grid is consistently refined ( $NI = 31 \times NJ = 71$ , where  $NI, NJ$  – O-type mesh number of nodes along radial coordinate (normal to the surface) and along surface). The translational temperature and six temperatures, which characterize vibration of N<sub>2</sub>, O<sub>2</sub>, CO<sub>2</sub>

(deformation, symmetric and asymmetric modes). On fig. 2d temperature profiles comparison for three type of grids is depicted. The presented data shows a good agreement of the results at crucial line for consistently grid refinement. But, as it is possible to see from fig. 1a, the grid adaptation near flowing surface becomes as coarser, as far from the front crucial line. This leads to greater inaccuracy of flow field definition near the back crucial line. This fact is illustrated on fig. 3: the distribution of convective fluxes along flowing surface from the front up to back crucial line is shown. It appears that with mesh refinement, the value of flux near front crucial line changes slightly, but the flux value near back crucial line increase more than an order. The integral fluxes distribution response along the whole surface of SV appears to be much fewer. (see fig.3a -3c).

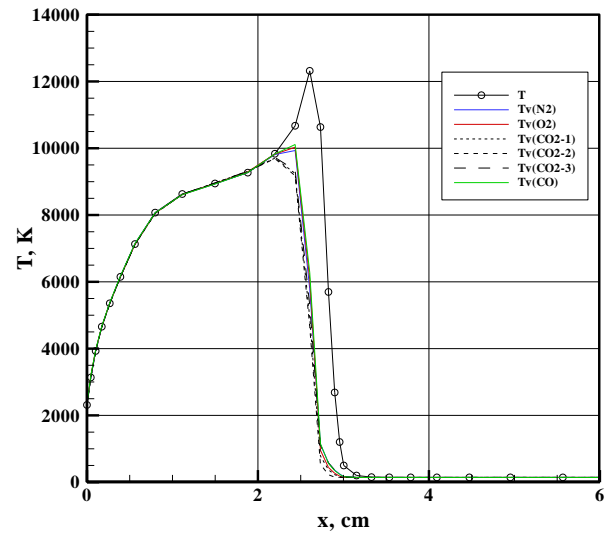


Fig. 2a. The distribution of translational and vibrational temperature along front crucial line at CO<sub>2</sub> and N<sub>2</sub> sphere flow at trajectory point  $t=52$  s. Mesh 31x71 nodes.

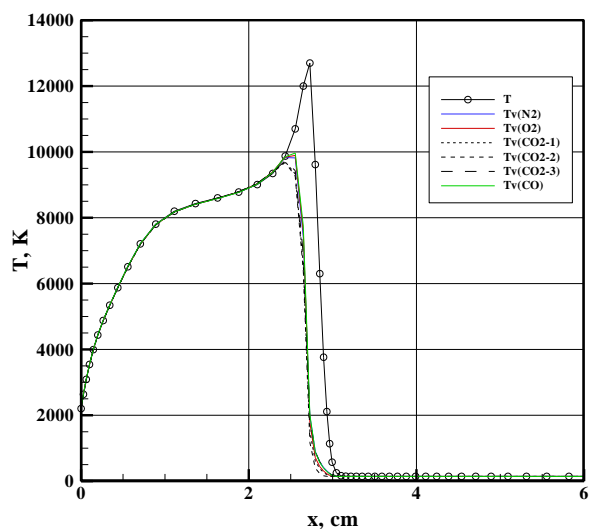


Fig. 2b. The distribution of translational and vibrational temperature along front crucial line at  $\text{CO}_2$  and  $\text{N}_2$  sphere flow at trajectory point  $t=52$  s. Mesh  $61 \times 141$  nodes.

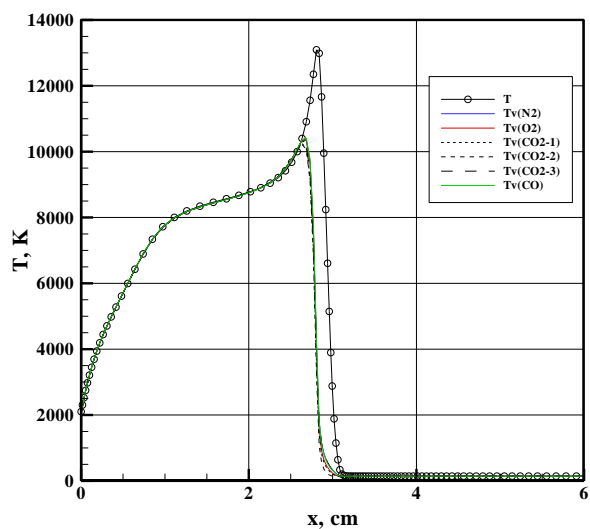


Fig. 2c. The distribution of translational and vibrational temperature along front crucial line at  $\text{CO}_2$  and  $\text{N}_2$  sphere flow at trajectory point  $t=52$  s. Mesh  $121 \times 281$  nodes.

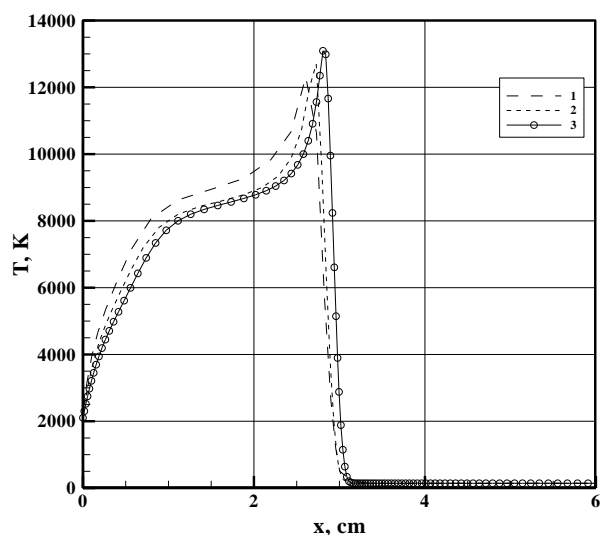


Fig. 2d. Temperature profiles comparison for different grids.

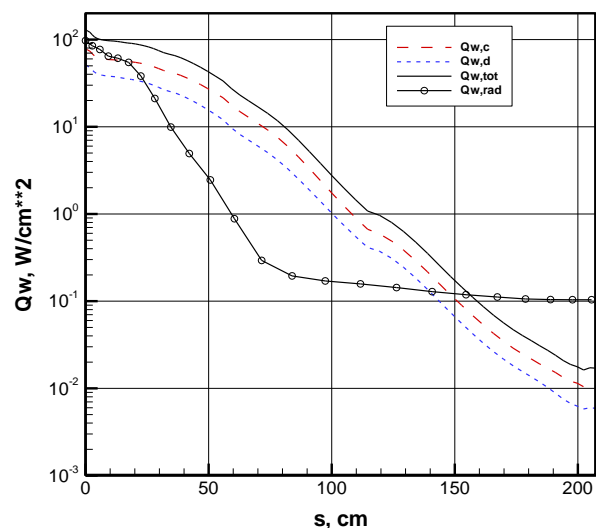


Fig. 3a. The distribution of convective fluxes along flowing surface from the front up to back crucial line for  $\text{CO}_2$ - $\text{N}_2$  mixture at trajectory point  $t=52$  c. Mesh  $31 \times 71$  nodes. The full kinetic model № 3. The dashed line – heat conductive and diffusing components.

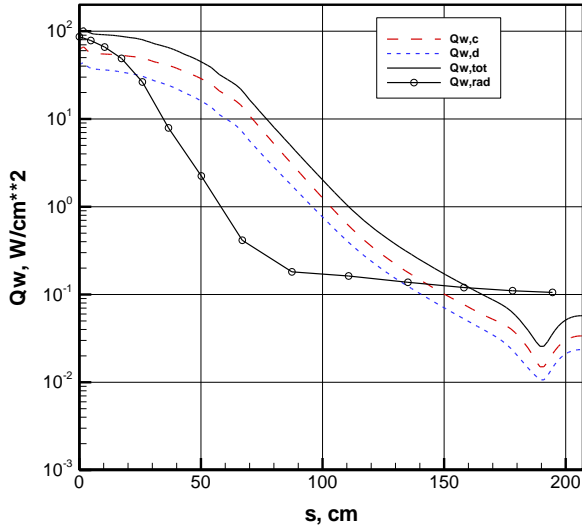


Fig. 3b. The distribution of convective fluxes along flowing surface from the front up to back crucial line for  $\text{CO}_2\text{-N}_2$  mixture at trajectory point  $t=52$  s. Mesh  $61 \times 141$  nodes. The full kinetic model № 3. The dashed line – heat conductive and diffusing components.

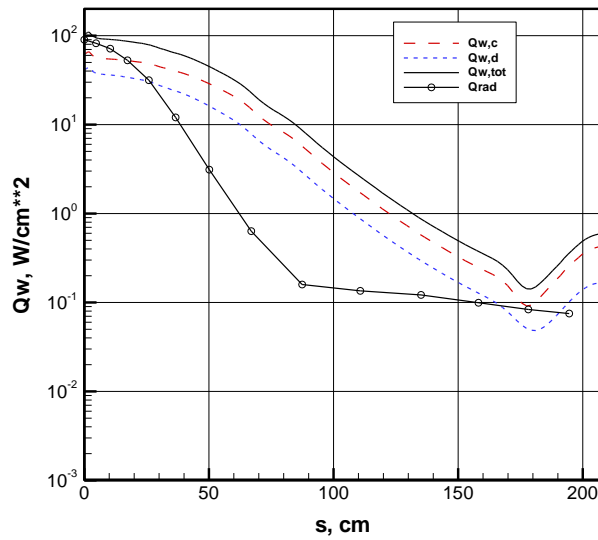


Fig. 3c. The distribution of convective fluxes along flowing surface from the front up to back crucial line for  $\text{CO}_2\text{-N}_2$  mixture at trajectory point  $t=52$  s. Mesh  $121 \times 281$  nodes. The full kinetic model № 3. The dashed line – heat conductive and diffusing components.

The crucial fact about comparability of convective and radiative fluxes to the surface appears from fig. 3a-3c. This is true for entering conditions for SV in atmosphere with  $\text{CO}_2$  (Mars, Venus). The considered point is characterized with significant disequilibrium of chemical process and shock layer structure (the characteristic size is close to boundary layer and relaxation zone behind the shock wave head). The central part of collapsed layer with temperature from ~

8500 up to 9500 K takes more than a half of the whole compressed layer. The thick of boundary layer is approximately 1 cm, and the thick of relaxation zone ~ 0.5 cm. That is why the calculation of heating in perturbed are has to be made using partially thermodynamic equilibrium. In this model the local thermodynamic approximation can be used for translational, translational-rotational and vibrational temperatures for two and three atomic molecules apart. The distribution of spectral radiative fluxes at six points at the surface of flowing sphere is shown on fig. 4. The point coordinates along surface are relevant to the whole length of semi-sphere moving line  $S_t=207$  cm. Cumulative functions of radiative fluxes are shown on. fig. 5.

Spectral radiation flux,  $\text{W}^*\text{cm/cm}^{**2}$

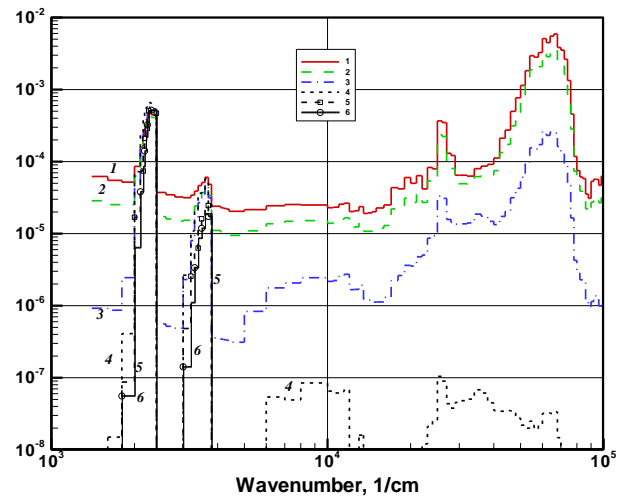


Fig. 4. Spectral radiative fluxes at six points on the sphere surface: 1 –  $s/S_t = 0$ ; 2 –  $s/S_t = 0.0854$ ; 3 –  $s/S_t = 0.256$ ; 4 –  $s/S_t = 0.569$ ; 5 –  $s/S_t = 0.863$ ; 6 –  $s/S_t = 0.983$

Integral Radiation Flux,  $\text{W/cm}^{**2}$

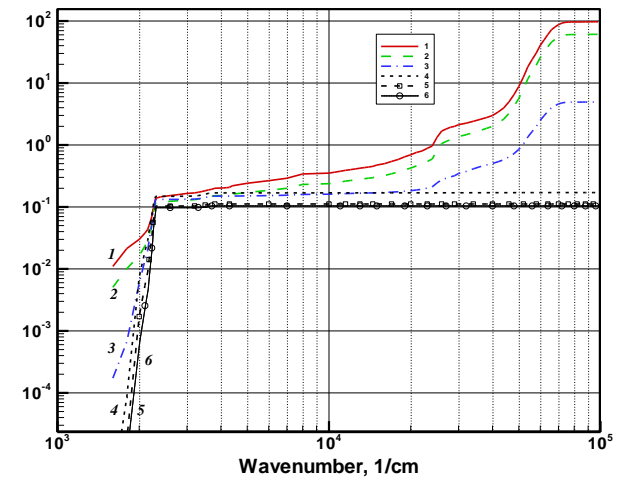


Fig. 5. Cumulative function of integral radiative flux at six points on sphere surface: 1 –  $s/S_i = 0$ ; 2 –  $s/S_i = 0.0854$ ; 3 –  $s/S_i = 0.256$ ; 4 –  $s/S_i = 0.569$ ; 5 –  $s/S_i = 0.863$ ; 6 –  $s/S_i = 0.983$

The spectral composition, which hits the surface, changes as far from front crucial line. Near the front crucial line (curves 1-3 on fig. 4) the radiation in visible and near UV spectrum ranges ( $\omega \in [40000-80000] \text{ cm}^{-1}$ ) is the bulk part of integral flux. At points 4-6 the surface is heating only with infrared  $\text{CO}_2$  and CO radiation. The distribution of cumulating functions tells just the same. The contribution of infrared radiation for the front crucial line ( $\omega < 20000 \text{ cm}^{-1}$ ) is less than 1%, (fig.5). More than 50% of integral flux is formed at ( $\omega > 40000 \text{ cm}^{-1}$ ). The contribution of visible and UV subranges of spectrum becomes smaller as far from front crucial line, thus almost 100% of integral flux at points 4-6 is formed at ( $\omega < 2300 \text{ cm}^{-1}$ ).

The analysis of optically active mixture components has to forego before detailed analysis of spectral radiative diffusion in compressed layer distribution. The mass fraction of gases mixture component along front crucial line is shown on fig. 6.

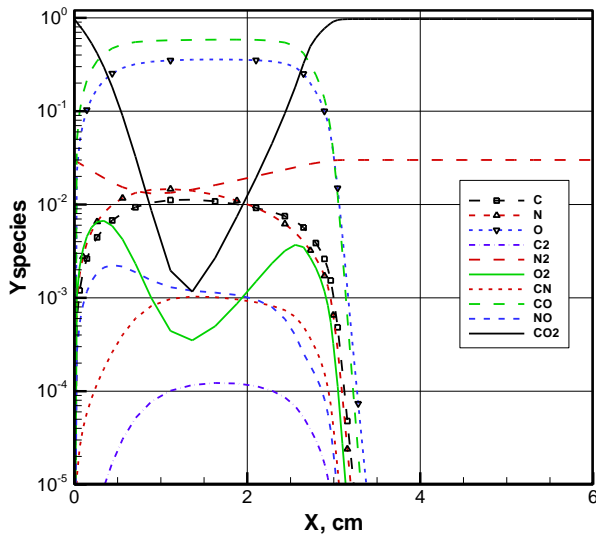


Fig. 6. The mass fraction of  $\text{CO}_2$ - $\text{N}_2$  mixture component along front crucial line at trajectory point  $t=52 \text{ s}$ . Mesh  $121 \times 281$  nodes.

Pay attention on significant concentrations of CO and  $\text{N}_2$  molecules in compressed layer, and on meaningful level of CN and NO radical concentrations, which (see. table.2), have series of quite intensive electronic-vibrational bands. The spectral distribution of radiative fluxes on the flowing SV surface are defined with spectral emitting and absorption ability fields and, also, specific of nonlinear radiative transfer process.

According to (10), radiation ability is defined with local value of absorption ability and Plank function. On fig. 7a and 7b the spectral absorption coefficient distribution in compressed layer near front (a) and back (b) crucial line. Molecules  $\text{N}_2$  - (1),  $\text{N}_2$ , CO, NO, CN - (2),  $\text{CO}_2$ , CO - (3) emits at different subranges of spectrum range. It follows from fig 7a, that absorption ability has maximum in the flowing sphere boundary layer. The absorption coefficient peak (3) is conditioned by absorption  $\text{CO}_2$ , particularly. In the neighborhood of back crucial line the significant absorption is observed in the whole area from near-by up to distant zone.

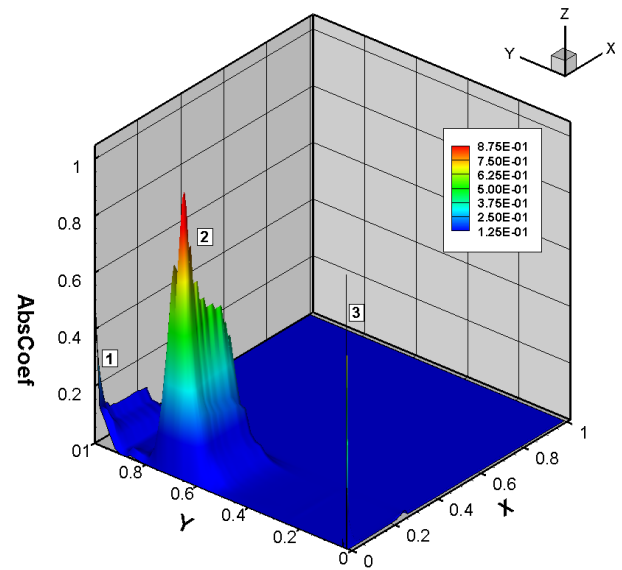


Fig. 7a. Spectral absorption coefficient distribution in compressed layer near non-catalytic surface along front (a) and back (b) crucial line;  $Y$  - relative radiation wave number,  $Y = (\omega_{\max} - \omega_{\min}) / \omega_{\max}$ ,  $\omega_{\min} = 1500 \text{ 1/cm}$ ,  $\omega_{\max} = 100000 \text{ 1/cm}$ ;  $X$  - relative physical coordinate, counted from surface towards incoming stream,  $X = x/x_{\max}$ ,  $x_{\max} = 10 \text{ cm}$

Have a look on emitting ability for compressed layer (a) and for trace, shown on fig. 8a and 8b. It becomes clear that the significant emitting ability is observed only in visible and near UV region. Infrared vibrational bands of  $\text{CO}_2$  radiate only in trace. In this case the emitting of molecules  $\text{N}_2$  - (1),  $\text{N}_2$ , CO, NO, CN - (2),  $\text{C}_2$ , CN - (3),  $\text{CO}_2$ , CO - (4) becomes significant. The mentioned trend becomes clear, taking into account Wien displacement law: there is an unambiguous link between Planks function maximum and temperature:  $\lambda_{\max} T = 2898 \text{ } \mu\text{m} \cdot \text{K}$ .

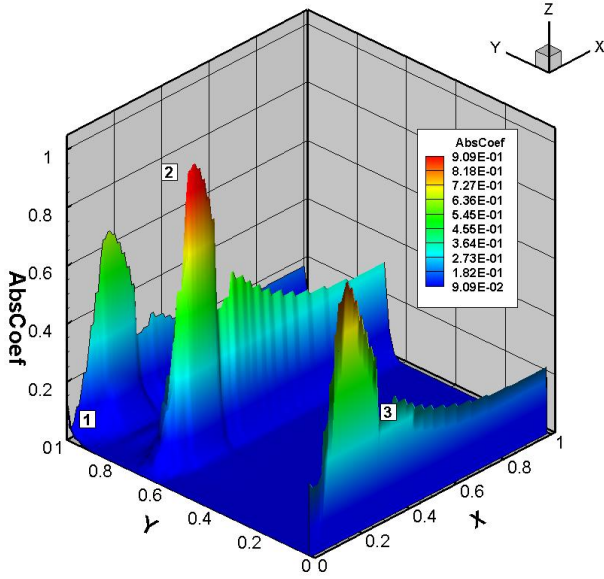


Fig. 7b. Spectral absorption coefficient distribution in compressed layer near non-catalytic surface along front (a) and back (b) crucial line;  $Y$  - relative radiation wave number,  $Y = (\omega_{\max} - \omega_{\min})/\omega_{\max}$ ,  $\omega_{\min} = 1500$  1/cm,  $\omega_{\max} = 100000$  1/cm;  $X$  - relative physical coordinate, counted from surface towards incoming stream,  $X = x/x_{\max}$ ,  $x_{\max} = 800$  cm.

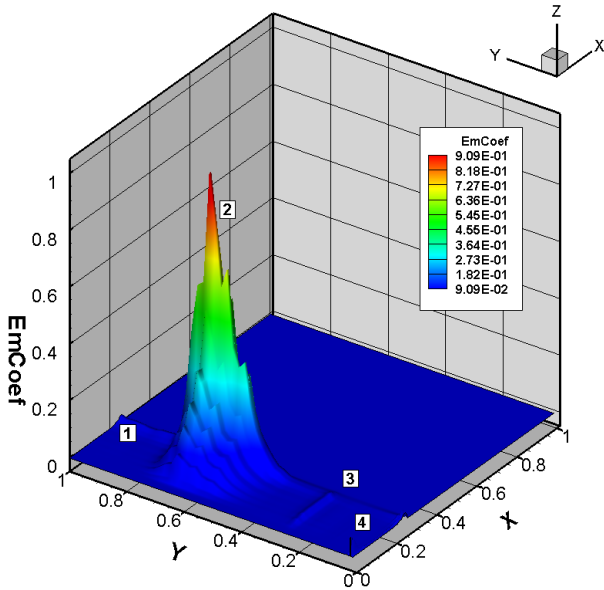


Fig. 8a. Spectral emitting coefficient distribution in compressed layer near non-catalytic surface along front (a) and back (b) crucial line;  $Y$  - relative radiation wave number,  $Y = (\omega_{\max} - \omega_{\min})/\omega_{\max}$ ,  $\omega_{\min} = 1500$  1/cm,  $\omega_{\max} = 100000$  1/cm;  $X$  - relative physical coordinate, counted from surface towards incoming stream,  $X = x/x_{\max}$ ,  $x_{\max} = 10$  cm.

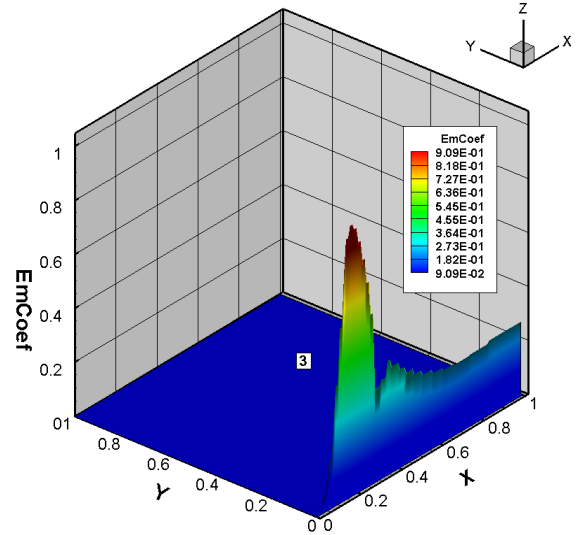


Fig. 8b. Spectral emitting coefficient distribution in compressed layer near non-catalytic surface along front (a) and back (b) crucial line;  $Y$  - relative radiation wave number,  $Y = (\omega_{\max} - \omega_{\min})/\omega_{\max}$ ,  $\omega_{\min} = 1500$  1/cm,  $\omega_{\max} = 100000$  1/cm;  $X$  - relative physical coordinate, counted from surface towards incoming stream,  $X = x/x_{\max}$ ,  $x_{\max} = 800$  cm.

In conclusion let us discuss the conceptual questions. The flowing CV calculation under assumption of Navier-Stokes equation becomes more complicated while calculation area increasing. Even taking into account the laminar types of flow one possible to observe numerical features: the result dependence from mesh specification and topology. The penalty of accuracy is observed even with mesh refinement (watching the solution stability at the same time, of itself). That is why the results have to be methodically checked every time (results converging from mesh adaptation, numerical and artificial disturbance, different mesh topology).

Generally noting the satisfying mesh convergence, the least reliable results are the distribution of convective flux on back semi-sphere surface. The accuracy increasing leads to specific mesh adaptation near back crucial line.

The analysis of the results for three trajectory points shows the gradual transition from significantly disequilibrium ( $t = 42$  s) up to almost equilibrium ( $t = 66$  s) conditions. The maximal convective heating is observed for quasi equilibrium trajectory point ( $t = 66$  s). The shift of heating maximum for trajectory points with significant proportion of disequilibrium ( $t \leq 52$  s) makes demands of more accurate radiation transfer under disequilibrium conditions.

### 3. CONCLUSION



The numerical-theoretical calculation of spherical SV radiative-convective heat exchange in the CO<sub>2</sub>-N<sub>2</sub> atmosphere for heat-stressed points of trajectory of Pathfinder is performed.

The distributions of radiative and convective fluxes along spherical SV surface (with the radius  $R = 66$  cm) at trajectory point corresponded to entering in Martian atmosphere at disequilibrium conditions are found out. At separate trajectory parts of SV entering in CO<sub>2</sub> atmosphere the radiation heating may exceed convective heating. The analysis of radiation flux value along the whole Martian SV surface is strongly required.

The analysis of spectral radiative flux to surface was performed. For this purpose the distribution of absorbing and emitting ability within the shock layer near front crucial line and in trace of flowing body was studied. The radiative heating under considered conditions is conditioned by emitting in electronic bands of CO (fourth positive system of bands and band Hopfield-Burge) and rotational-vibrational CO<sub>2</sub> bands. It is important to remark that calculations are made under assumption of local thermodynamic equilibrium. The significant part of Martian SV trajectory are hold in rarefied atmosphere, so the future code development is to be taken into account.

This work is performed under Program of Basic Research RAS (investigation of physical-chemical model of hypersonic flows), project RFBR № 10-01-00544 (in terms of development of computer models of radiation gas dynamics of spacecraft) and № 09-08-92422-K3\_a (joint project of RFBR – Consortium E.I.N.S.T.E.I.N. (Italy), in analyzing the patterns of radiation energy transfer). The values of radiative and convective flux used for shock wave tube experiments planning in Laboratory of Physical Kinetics of MIPT (project RFBR № 10-01-00468) and Lomonosov's Research Institute of Mechanics (project RFBR № 09-08-00272).

#### 4. REFERENCES

1. Milos F.S., Chen Y.-K., Gongdon W.M., Thornton J.M. *Mars Pathfinder Enter Temperature Data, Aerothermal Heating, and Heatshield Material Response*, Journal of Spacecraft and Rockets, 1999. V. 36. №3. P.380.
2. Anfimov N.A., Dem'yanov Y.A. Zavernyaev Y.A., etc., *On the measurement of some parameters of planetary atmospheres by radiation accompanying the flight re-entry vehicles at the site of inhibition*, Math. USSR. Fluid Dynamics. 1981. № 1. p. 36.
3. Gulard R., Bugner R.E., Burns R.K., Nelson G.F., *The flow of radiating gas in a planetary entry*, TVT. 1969. Vol. 7. № 3. p. 542.
4. Karasev A.B., Lyakh A.N., *Study of radiative and convective heat transfer in a critical point of the radiating a mixture of carbon dioxide and nitrogen*, Math. USSR. Fluid Dynamics. 1971. № 2. P.39.
5. Page W.A., Woodward H.T., *Radiative and Convective Heating during Venus Entry*, AIAA J. 1972. Vol.10. № 10. P.1379.
6. Golovachev J.P., *The heat exchange in the forward stagnation point of a blunt body under flow emitting a mixture of carbon dioxide and nitrogen*, Moscow, TVT. 1975. T.13. № 5. S.1029.
7. Golovachev Y.P., Popov F.D., *The flow around blunted cones at the entrance to the atmosphere, consisting of carbon dioxide and nitrogen*, Math. USSR. Fluid Dynamics. 1975. № 2. S.175.
8. Surzhikov S.T. 2D CFD/RadGD Model of Space Vehicles, *Proc. 1st Int. Workshop on Radiation of High Temperature Gases in Atmospheric Entry*. ESA SP-533. Lisbon, Portugal. 2003. P.95.
9. Surzhikov S.T., *TC3: Convective and Radiative Heating of MSRO for Simplest Kinetic Models*, Proc. Int. Workshop on Radiation of High Temperature Gases in Atmospheric Entry. Part II. ESA SP-583. Porquerolles. France. 2005. P.55.
10. Surzhikov S.T., *Two-dimensional radiation-gasdynamic model Aerophysics reentry spacecraft. Proc.: Actual problems of mechanics. Fluid mechanics, gas and plasma*, Moscow, Nauka, 2008. p. 20.
11. Surzhikov S.T., *Numerical Simulation of Heat Radiation Generated by Entering Space Vehicle*, AIAA Paper 04-2379. 2009.
12. Bird R., Stuart W., Lightfoot E., *Transport Phenomena*. Moscow: Khimiya, 1974. 687 pp.
13. *Chemistry of Combustion*, Ed. Gardiner W. M.: Mir, 1988.
14. Ginzburg I.P., *Friction and heat transfer during the motion of the mixture of gases*. L.: Izd-vo LGU, 1975. 278 pp.
15. Anfimov N.A., *Laminar boundary layer in a multicomponent mixture of gases*, "Izv. USSR. Mechanics and mechanical engineering. 1962. № 1. p. 25.
16. Gurvich L.V., Veits I.V., Medvedev V.A. and other, *Thermodynamic properties of individual substances*, Moscow, Nauka, 1978. 495 pp.
17. Surzhikov S.T., *TC3: Convective and Radiative Heating of MSRO, Predicted by Different Kinetic Models*, Proceedings of the Second International Workshop on Radiation of High Temperature Gases in Atmospheric Entry. 6-8 Sept., 2006. Rome. Italy. – ESA SP-629. CD-format.
18. Surzhikov S.T., *Optical properties of gases and plasma*. Moscow, BMSTU, 2004
19. Surzhikov S.T., *Thermal radiation of gases and plasma*, Moscow, BMSTU, 2004
20. Edwards J.R., Liou M.-S., *Low-Diffusion Flux-Splitting Methods for Flow at all Speeds*, AIAA J. 1998. V. 36, № 9, P.1610.



Table 1. Vibrational modes characteristics

Vibrational mode number	Name	Characteristic vibrational temperature, $\theta_m$ , K	Molecular weight $M_{i(m)}$ , g/mole
1	vibrational mode $N_2$	3354	28
2	vibrational mode $O_2$	2240	32
3	symmetric vibrational mode $CO_2$	1999	44
4	antisymmetric vibrational mode $CO_2$	3383	44
5	deformation vibrational mode $CO_2$	960	44
6	vibrational mode CO	3084	30

Table 2. Electronic and vibrational band of diatomic molecules.

Molecule, the electronic transition, System name	Spectral range of observed bands system, $cm^{-1}$	Range of variation vibrational wave numbers of upper and lower states	
		$v'$	$v''$
$C_2, A^1\Pi_u - X^1\Sigma_g^+$ Phillips	100 ÷ 27000	15	15
$C_2, B'^1\Sigma_g^+ - A^1\Pi_u$	100 ÷ 22000	10	10
$C_2, B^1\Delta_g - A^1\Pi_u$	100 ÷ 17000	10	15
$C_2, b^3\Sigma_g^- - a^3\Pi_u$ Ballico – Ramsay	100 ÷ 20000	12	12
$C_2, C^1\Pi_g - A^1\Pi_u$ Delandr – D'Azambua	8000 ÷ 42000	10	15
$C_2, d^3\Pi_g - a^3\Pi_u$ Swann	3500 ÷ 35000	12	15
$C_2, D^1\Sigma_u^+ - X^1\Sigma_g^+$ Mulliken	38000 ÷ 48000	15	15
$C_2, E^1\Sigma_g^+ - A^1\Pi_u$	28000 ÷ 60000	10	15
$C_2, E^1\Sigma_g^+ - D^1\Sigma_u^+$	100 ÷ 23000	10	10
$C_2, e^3\Pi_g - a^3\Pi_u$ Fox – Herzberg	21000 ÷ 48500	10	12
$CN, A^2\Pi - X^2\Sigma^+$ Red	1000 ÷ 24000	15	15
$CN, B^2\Sigma^+ - A^2\Pi$	1000 ÷ 45000	15	15
$CN, B^2\Sigma^+ - X^2\Sigma^+$ Violet	17000 ÷ 37000	15	15
$CN, X^2\Sigma^+ - X^2\Sigma^+$	1000 ÷ 10000	25	25
$CO, a'^3\Sigma^+ - a^3\Pi$ Asundi	100 ÷ 20000	12	12
$CO, A^1\Pi - X^1\Sigma^+$ 4 - positive	30000 ÷ 85000	20	29
$CO, B^1\Sigma^+ - A^1\Pi$ Angstrom	5000 ÷ 52000	15	20
$CO, B^1\Sigma^+ - X^1\Sigma^+$ Hopfild – Burge	74000 ÷ 100000	15	25
$CO, b^3\Sigma^+ - a^3\Pi$ 3 – positive	16000 ÷ 51000	10	21
$CO, d^3\Delta - a^3\Pi$ Triplet	100 ÷ 28 000	15	12
$CO, e^3\Sigma^- - a^3\Pi$ Herman	100 ÷ 30000	15	12
$CO, X^1\Sigma^+ - X^1\Sigma^+$	100 ÷ 8000	25	25
$NO, A^2\Sigma^+ - X^2\Pi$ $\gamma$ - system	16000 ÷ 62000	8	22
$NO, B'^2\Delta - X^2\Pi$ $\beta'$ - system	35000 ÷ 68000	7	22
$NO, B^2\Pi - X^2\Pi$ $\beta$ - system	16000 ÷ 60000	15	22
$NO, C^2\Pi - A^2\Sigma^+$	1000 ÷ 20000	4	8
$NO, C^2\Pi - X^2\Pi$ $\delta$ - system	20000 ÷ 65000	4	22
$NO, D^2\Sigma^+ - A^2\Sigma^+$	3500 ÷ 15000	4	8
$NO, D^2\Sigma^+ - X^2\Pi$ $\varepsilon$ - system	20000 ÷ 65000	4	22
$NO, X^2\Pi - X^2\Pi$	100 ÷ 15000	25	25
$N_2, a^1\Pi_g - a'^1\Sigma_u^-$ Macfarlane	100 ÷ 20000	21	21
$N_2, A^3\Sigma_u^+ - X^1\Sigma_g^+$ Vegard Kaplan –	1000 ÷ 75000	21	21
$NO, D^2\Sigma^+ - X^2\Pi$ $\varepsilon$ - system	20000 ÷ 65000	4	22

NO, $X^2\Pi - X^2\Pi$	$100 \div 15000$	25	25
$N_2, b'^1\Sigma_u^+ - X'^1\Sigma_g^+$ Berge – Hopfild 2	$54000 \div 1200000$	25	25
$N_2, B'^3\Sigma_u^- - B^3\Pi_g$ «Y» - bands	$100 \div 20000$	21	21
$N_2, B^3\Pi_g - A^3\Sigma_u^+$ 1 - positive	$1000 \div 25000$	21	21
$N_2, a'^1\Pi_g - a'^1\Sigma_u^-$ Macfarlane	$100 \div 20000$	21	21
$N_2, A^3\Sigma_u^+ - X'^1\Sigma_g^+$ Vegard - Kaplan	$1000 \div 75000$	21	21
$N_2, B^3\Pi_g - A^3\Sigma_u^+$ 1 - positive	$1000 \div 25000$	21	21
$N_2, b^1\Pi_u - X'^1\Sigma_g^+$ Berge – Hopfild 1	$74000 \div 105000$	1	12
$N_2, W^3\Delta_u - B^3\Pi_g$ Bands Wu – Benes	$10 \div 20000$	21	21
$N_2, D^3\Sigma_u^+ - B^3\Pi_g$ 4 – positive	$28500 \div 50000$	0	10
$N_2, E^3\Sigma_g^+ - A^3\Sigma_u^+$	$30000 \div 50000$	1	10
$N_2, E^3\Sigma_g^+ - B^3\Pi_g$	$15000 \div 40000$	1	15
$N_2, E^3\Sigma_g^+ - C^3\Pi_u$	$500 \div 10000$	1	4
$N_2, C^3\Pi_u - B^3\Pi_g$ 2 – positive	$10000 \div 40000$	4	19
$O_2, B^3\Sigma_u^- - X^3\Sigma_g^-$ Schumann - Runge	$22000 \div 57000$	14	21

Table 3. Initial data for calculations.

Variant number	$t, s$	$V_\infty, \text{cm/s}$	$p_\infty, \text{erg/cm}^3$	$\rho_\infty, \text{g/cm}^3$	$T_\infty, K$	Re	$M_\infty$
1	45	0.749E+06	0.24620E+01	0.101E-07	129	0.560E+04	41.6
2	52	0.736E+06	0.15560E+02	0.576E-07	143	0.285E+05	38.9
3	66	0.660E+06	0.89410E+02	0.280E-06	169	0.106E+06	32.0